# The Sudbury Neutrino Observatory

A. Bellerive[a], J.R. Klein[b], A.B. McDonald[c,*], A.J. Noble[c], A.W.P. Poon[d], for the SNO Collaboration

[a] *Ottawa-Carleton Institute for Physics, Department of Physics, Carleton University, Ottawa, Ontario K1S 5B6, Canada*
[b] *Department of Physics and Astronomy, University of Pennsylvania, Philadelphia, PA 19104, USA*
[c] *Department of Physics, Queen's University, Kingston, Ontario K7L 3N6, Canada*
[d] *Institute for Nuclear and Particle Astrophysics, Nuclear Science Division, Lawrence Berkeley National Laboratory, Berkeley, CA 94720, USA*

arXiv:1602.02469v2 [nucl-ex] 22 Apr 2016

**Abstract**

This review paper provides a summary of the published results of the Sudbury Neutrino Observatory (SNO) experiment that was carried out by an international scientific collaboration with data collected during the period from 1999 to 2006. By using heavy water as a detection medium, the SNO experiment demonstrated clearly that solar electron neutrinos from $^8$B decay in the solar core change into other active neutrino flavors in transit to Earth. The reaction on deuterium that has equal sensitivity to all active neutrino flavors also provides a very accurate measure of the initial solar flux for comparison with solar models. This review summarizes the results from three phases of solar neutrino detection as well as other physics results obtained from analyses of the SNO data.

*Keywords:* Neutrinos, neutrino oscillations, Solar Neutrino Problem

## 1. Introduction

The Sudbury Neutrino Observatory (SNO) was initiated in 1984 primarily to provide a definitive answer to the Solar Neutrino Problem [1]. Ever since the pioneering calculations of solar neutrino fluxes by John Bahcall and the pioneering measurements by Ray Davis in the 1960's, it was known that there was a discrepancy between the observed fluxes and the calculations. The persistence of the problem motivated Herb Chen to contact Canadian scientist Cliff Hargrove, a former colleague, to explore whether there was a possibility that enough heavy water could be made available on loan to perform a sensitive measurement and determine whether the neutrinos change their type in transit from the core of the Sun. The unique properties of deuterium could make it possible to observe both the electron neutrinos produced in the core of the Sun and the sum of all neutrino types [2]. With

*Corresponding author
*Email addresses:* alainb@physics.carleton.ca (A. Bellerive), jrk@hep.upenn.edu (J.R. Klein), art@snolab.ca (A.B. McDonald), potato@snolab.ca (A.J. Noble), awpoon@lbl.gov (A.W.P. Poon)

the immediate involvement of George Ewan, who had been exploring underground sites for future experiments, a collaboration of 16 Canadian and US scientists was formed in 1984, led by Chen and Ewan as Co-Spokesmen [3]. UK scientists joined in 1985, led by David Sinclair as UK Spokesman.

An initial design was developed, to be sited 2 km underground in Inco's Creighton mine near Sudbury, Ontario, Canada and preliminary approval was obtained from Atomic Energy of Canada Limited (AECL) for the loan of 1000 tonnes of heavy water. Unfortunately Herb Chen passed away tragically from leukemia in 1987. The collaboration continued with Art McDonald and Gene Beier as US Spokesmen and grew with the addition of other institutions in the US and Canada for a total of 13 institutions. In 1989, funding was provided jointly by Canadian, US and UK agencies and McDonald became Director of the project and the scientific collaboration.

## 2. Science of Solar Neutrinos and Detection by SNO

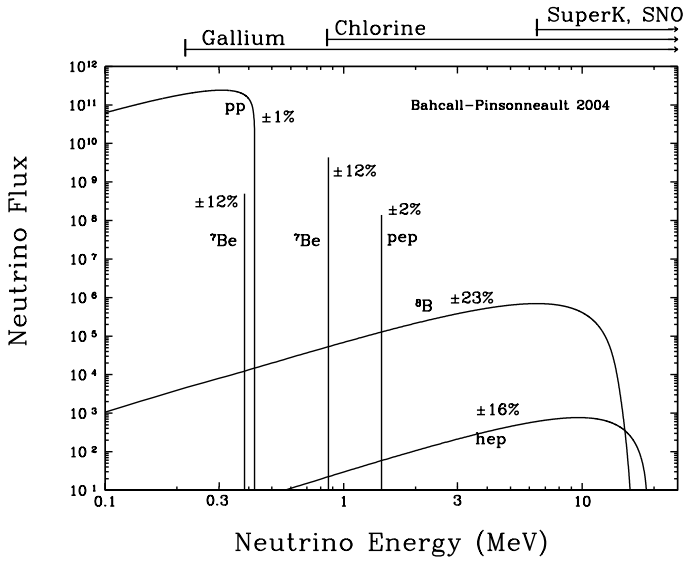


Figure 1: Fluxes of neutrinos from the pp chain in the Sun. Threshold energies for neutrino detection using chlorine, gallium and $H_2O$ (Kamiokande and Super-Kamiokande experiments) are shown.

Figure 1 shows the fluxes of neutrinos from the pp chain reactions that comprise the principal power source in the Sun [4]. Overall the series of reactions can be summarized as: $4\mathrm{p} \rightarrow {}^4\mathrm{He} + 2e^+ + 2\nu_e + 26.73$ MeV. Also shown are the thresholds for neutrino detection for the chorine, gallium and $H_2O$-based experiments that took place before the SNO results were first reported in 2001. These experiments were either exclusively (chlorine, gallium) or predominantly ($H_2O$) sensitive to the electron-type neutrinos produced in the Sun. They

all showed deficits of factors of two to three compared to the fluxes illustrated in Fig. 1. It was not possible, however, for these experiments to show conclusively that this was due to neutrino flavor change rather than defects in the solar flux calculations. With heavy water containing deuterium ($D_2O$), the SNO experiment was able to measure two separate reactions on deuteron (d):

1. $\nu_e + \mathrm{d} \rightarrow \mathrm{p} + \mathrm{p} + e^-$, a charged current (CC) reaction that was sensitive only to electron-flavor neutrinos, and
2. $\nu_x + \mathrm{d} \rightarrow \mathrm{n} + \mathrm{p} + \nu_x$, a neutral current (NC) reaction that was equally sensitive to all neutrino types.

A significant deficit in the $^8$B $\nu$ flux measured by the CC reaction over that measured by the NC reaction would directly demonstrate that the Sun's electron neutrinos were changing to one of the other two types, without reference to solar models. At the same time, the NC reaction provided a measurement of the total flux of $^8$B solar neutrinos independent of neutrino flavor change. The CC reaction was detected by observing the cone of Cherenkov light produced by the fast moving electron. The NC reaction was detected in three different ways in the three phases of the project. In Phase I, with pure heavy water in the detector, the NC reaction was observed via Cherenkov light from conversion of the 6.25-MeV $\gamma$ ray produced when the free neutron captured on deuterium. In Phase II, with NaCl dissolved in the heavy water, the neutrons produced via the NC reaction captured predominantly on chlorine, resulting in a cascade of $\gamma$ rays with energy totaling 8.6 MeV and producing a very isotropic distribution of light in the detector. The capture efficiency was increased significantly during Phase II and the isotropy enabled a separation of events from the two reactions on a statistical basis. In Phase III, the NC neutrons were detected in an array of $^3$He-filled neutron counters.

In addition, the SNO detector could observe neutrinos of all flavors via the elastic scattering (ES) of electrons by neutrinos:

3. $\nu_x + e^- \rightarrow \nu_x + e^-$ which is six times more sensitive to electron neutrinos than other flavors.

This is the same reaction used by the Kamiokande-II and Super-Kamiokande experiments to observe solar neutrinos using light water as a medium.

## 3. Experiment Description

Figure 2 is a schematic diagram of the SNO detector [5]. The cavity was 34 meters high by 22 meters in diameter at the equator, lined with a water- and radon-impermeable Urylon plastic. The detector was situated 2 km underground in an active nickel mine owned by Vale (formerly Inco Ltd) near Sudbury, Ontario. The central element was 1000 tonnes of heavy water ($> 99.5\%$ isotopically pure), on loan from AECL and housed in a transparent acrylic vessel (AV) 12 meters in diameter and 5 cm thick. The value of the heavy water was about $300 million Canadian dollars. The heavy water was viewed by 9438 20-cm diameter Hamamatsu R1408 photomultiplier tubes (PMT) mounted on a stainless steel

geodesic photomultiplier support frame (PSUP). Each PMT had a 27-cm entrance light concentrator to increase the effective photocathode coverage to 54%. A further 91 PMTs without concentrators were mounted looking outward from the PSUP to observe events entering the detector from the outside. The entire cavity outside the acrylic vessel was filled with 7000 tonnes of ultra-pure ordinary water.

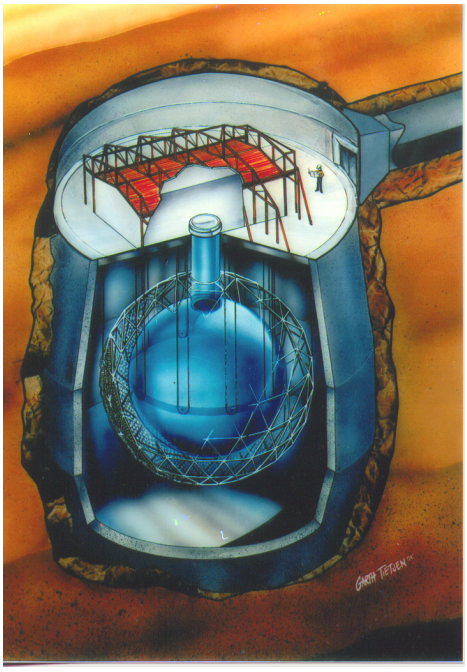

Figure 2: Schematic cutaway view of the SNO detector suspended inside the SNO cavity.

The construction sequence involved the building of the upper half of the geodesic structure for the PMTs, installing them and lifting it with a movable platform into place. This was followed by the construction of the upper half of the acrylic vessel, which was a major process, involving the bonding together of the first half of the 122 panels that were smaller than the maximum length of 3.9 meters that could fit within the mine hoist cage. The platform was then moved down by stages with the lower half of the acrylic vessel and the PMT structure added sequentially.

Calibration was accomplished using a set of specialized sources that could be placed on the central axis or on two orthogonal planes off-axis in locations that covered more than 70% of the detector. These sources included 6.13-MeV $\gamma$ rays triggered from decays of $^{16}$N [6], a source of $^{8}$Li [7], encapsulated sources of U, Th, a $^{252}$Cf fission neutron source, 19.8-MeV $\gamma$ rays from the t(p,$\gamma$) reaction generated by a small accelerator suspended on the central axis [8]. The $^{16}$N and $^{8}$Li were produced by a d(t,n) neutron source generated by a small accelerator in a location near the SNO detector and transported by capillary tubes to the main heavy water volume.

Signals from the SNO PMTs were received by electronics that made four different mea-

surements. For all PMT signals that were above a threshold of the equivalent of 1/4 of a photoelectron of charge, the electronics recorded a time relative to a global trigger, and provided three different charge measurements: a short-window (60 ns) integration of the PMT pulse, a long-window ($\sim$ 400 ns) integration, and a low-gain version of the long-integration charge. Each PMT above 1/4 pe also provided a 93 ns-wide analog trigger signal and signals across the entire detector were summed together. An event was triggered if that sum exceeded a pre-set threshold, representing a number of PMTs firing in coincidence. The system also kept absolute time according to a GPS clock signal that was sent underground.

An accurate determination of the total solar neutrino flux required a detector with ultra-low levels of any radioactive sources capable of mimicking the signal. In addition, the residual levels needed to be determined with sufficient accuracy that they contribute only slightly to the overall measurement uncertainties. Of particular concern for SNO were two high-energy $\gamma$ rays produced in the $^{232}$Th and $^{238}$U chains (of energy 2615 and 2447 keV, respectively). These were above the deuteron photo-disintegration threshold and hence produce neutrons indistinguishable from neutrino induced events. As a consequence, all the materials used in the fabrication of the detector were carefully screened for radioactivity and the collaboration worked with manufacturers to develop techniques to produce radioactively pure materials and components.

To achieve this level of radiopurity in the water, both the light and heavy water in SNO were purified through numerous stages including filtration, degassing, customized ion-exchange and reverse osmosis. The $H_2O$ and $D_2O$ purification plants were designed to remove Rn, Ra, Th and Pb from the water, thereby eliminating sources giving rise to the high energy $\gamma$ rays. Two of the main elements of the SNO $H_2O$ and $D_2O$ purification plants consisted of newly developed ion-exchange processes using MnOx [9] and HTiO [10], which targeted Ra, Th, and Pb nuclei in the water. With the removal of these elements, secular equilibrium was broken and the short lived daughters quickly decayed away. The HTiO and MnOx techniques developed by SNO were also used to assay the amount of residual activity remaining in the fluids. In the case of HTiO, the activity was eluted from HTiO by strong acids and concentrated into liquid scintillator vials for counting. The technique developed for MnOx used electrostatic counters to measure the $^{222}$Rn and $^{220}$Rn emanating from the surface.

Radon gas was particularly problematic as it emanated from materials and could migrate or diffuse into sensitive areas of the detector. Large process degassers and membrane contactors were used to strip radon from the water with high efficiency. Monitoring degassers were used to collect radon from the water into Lucas cells for a determination of the residual contamination.

The design of the purification systems was to achieve a rate of photo-disintegration events created by impurities of less than 10% of the NC rate predicted by the Standard Solar Model. To achieve this in the $D_2O$ system required an equivalent of $< 3.8 \times 10^{-15}$gTh/g$D_2O$ and $< 3.0 \times 10^{-14}$gU/g$D_2O$. The requirements for the $H_2O$ outside the main detector were not as stringent, and were $< 37 \times 10^{-15}$gTh/g$H_2O$ and $< 45 \times 10^{-14}$gU/g$H_2O$. Measurements of the water purity throughout the experiment showed that the levels for U in both $D_2O$ and $H_2O$, and Th in $D_2O$ were consistently better than the design value, while the Th content in $H_2O$

was about at the target level. Hence the background contamination rate was not significant in comparison to the neutrino NC signal. The assay measurements were consistent between HTiO, MnOx and radon gas measurements, and agreed with *in-situ* measurements made with the PMT array.

## 4. SNO Phase-I Physics Program

SNO's first measurements of the rates of CC and NC reactions on deuterium by $^8$B solar neutrinos used unadulterated $D_2O$ in the detector. The measurements had several challenges that differed from the following two phases of the experiment. The first was that the number of detected events expected from the NC reaction was low, in part because the neutron capture cross section on deuterium is small, but also because the energy of the $\gamma$ ray released in that capture was just 6.25 MeV, near SNO's anticipated energy threshold. The Phase-I data analysis was also the first to face unexpectedly large instrumental backgrounds, which had to be removed before more detailed analyses could proceed. The primary result from Phase I was a rejection of the null hypothesis that solar neutrinos do not change flavor by comparing the flux measured by the CC reaction to those by both NC and ES reactions.

In SNO Phase I, the signals from the ES, CC, and NC reactions could not be separated on an event-by-event basis. Instead, a fit to the data set was performed for each signal amplitude, using the fact that they are distributed distinctly in the following three derived quantities: the effective kinetic energy $T_{\rm eff}$ of the $\gamma$ ray resulting from the capture of a neutron produced by the NC reaction or of the recoil electron from the CC or ES reactions, the reconstructed radial position of the interaction ($R_{\rm fit}$) and the reconstructed direction of the event relative to the expected direction of a neutrino arriving from the Sun ($\cos\theta_\odot$). The reconstructed radial positions $R_{\rm fit}$ were measured in units of AV radii and weighted by volume, so that $\rho \equiv (R_{\rm fit}/R_{\rm AV})^3 = 1.0$ when an event reconstructs at the edge of the $D_2O$ volume.

Figure 3 shows the simulated distributions for each of the signals. The nine distributions were used as probability density functions (PDFs) in a generalized maximum likelihood fit of the solar neutrino data. The top row shows the $T_{\rm eff}$ distribution for each of the three signals. The CC and ES reactions both reflect the $^8$B spectrum of incident neutrinos, with ES having a much softer spectrum due to the kinematics of the reaction. The NC reaction is essentially a line spectrum, because neutron capture on deuterium always results in the same 6.25-MeV $\gamma$ ray. The $\rho$ distributions are shown in the middle row of Fig. 3. Electrons from the CC reaction are distributed only within the heavy water volume, while those from ES extend into the light water. The neutrons from the NC reaction fall nearly linearly in $\rho$ from the center of the heavy water to the edge, because of the probability of exiting the heavy water volume and being captured on light water (and thus being below the detection threshold). The bottom row of Fig. 3 shows the $\cos\theta_\odot$ distribution of the events. The ES reaction has a prominent peak indicating the solar origin for the neutrinos. The CC electrons have a softer but nonetheless distinctive $\sim (1 - 1/3\cos\theta_\odot)$ distribution, while the NC neutrons have no correlation at all with the solar direction.

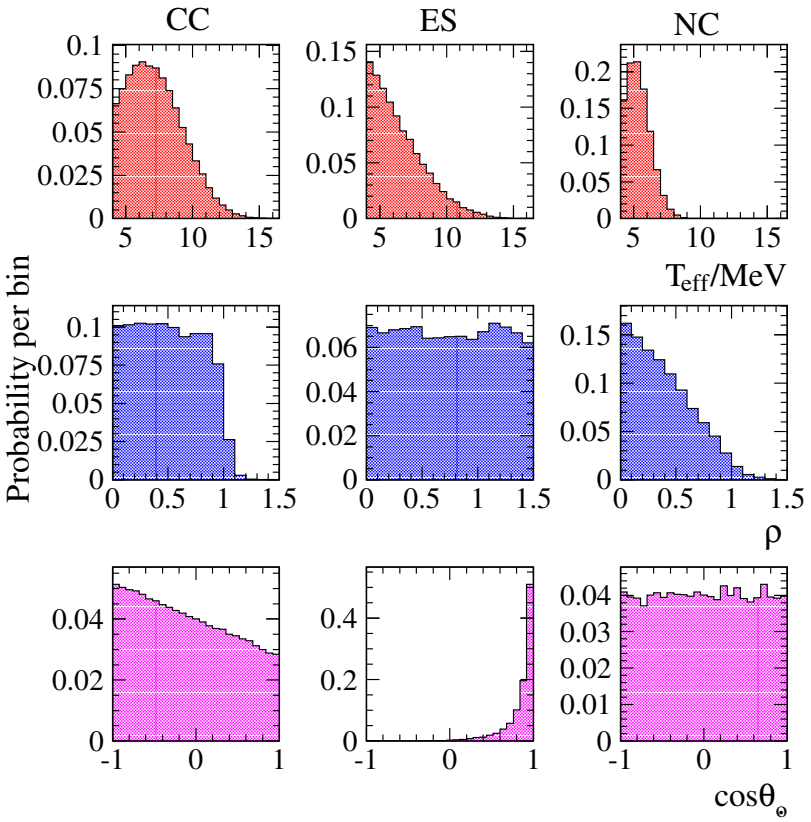


Figure 3: The energy (top row), radial (middle row), and directional (bottom row) distributions used to build PDFs to fit the SNO signal data. $T_{\rm eff}$ is the effective kinetic energy of the $\gamma$ from neutron capture or of the electron from the ES or CC reactions, and $\rho = (R_{\rm fit}/R_{\rm AV})^3$ is the reconstructed event radius, volume-weighted to the 600 cm radius of the acrylic vessel.

The Phase-I data set was acquired between November 2, 1999 and May 31, 2001, and represented a total of 306.4 live days. The SNO detector responded to several triggers, the primary one being a coincidence of 18 or more PMTs firing within a period of 93 ns (the threshold was lowered to 16 or more PMTs after December 20, 2000). The rate of such triggers averaged roughly 5 Hz. A "random" trigger also pulsed the detector at 5 Hz throughout the data acquisition period.

To provide a final check against statistical bias, the data set was divided in two: an "open" data set to which all analysis procedures and methods were applied, and a "blind" data set upon which no analysis within the signal region (between 40 and 200 hit PMTs) was performed until the full analysis program had been finalized. The blind data set began at the end of June 2000, at which point only 10% of the data set was being analyzed, leaving the remaining 90% blind. The total size of the blind data set thus corresponded to roughly 30% of the total live time.

The presence of many sources of events created by the instrumentation of the SNO

detector was apparent even before the start of heavy water running. The approach to removing these events began with a suite of simple cuts to act as a series of "coarse filters," removing the most obvious of such events, before any event reconstruction. Sources of instrumental events included light generated by the PMTs ("flasher PMTs") that happened for every PMT and occurred at a rate of roughly 1/minute; light from occasional high-voltage breakdown in the PMT connector or base; light generated by static discharge in the neck of the vessel; electronic pickup; and isotropic light occasionally emitted by the acrylic vessel. The cuts were based only on simple low-level information such as PMT charges and times, but the full suite removed the vast majority of the instrumental events. Two independent suites were created to help validate the overall performance of the coarse filters. The acceptance for signal events of the instrumental background cuts was measured using calibration source data, and was found to be >99.5%.

The reconstruction of event position, direction, and energy was performed on events that passed the instrumental background cuts. Position reconstruction used the relative PMT-hit times as well as the angular distribution of photon hits about a hypothesized event direction. Event energy used the number of PMT hits along with an analytic model of the detector response to Cherenkov light that was a function of event position and direction. For both position and energy, additional independent algorithms were used to validate the results [11].

After reconstruction, a further set of cuts were applied to remove events that were not consistent with the timing and angular distribution of Cherenkov light ("Cherenkov Box Cuts"). The two cuts that defined the Cherenkov Box were the width of the prompt timing peak of the PMT hits, and the average angle between pairs of hit PMTs.

Neutrons and events from spallation products that were created by the passage of muons or the interactions of atmospheric neutrinos were removed by imposing a 20-s veto window following the muon events, and a 250-ms veto following any event that produced more than 60 fired PMTs (roughly 7 MeV of electron-equivalent total energy $E_{\rm eff}$). The final set of cuts were the requirement that events have a reconstructed effective kinetic energy $T_{\rm eff} = E_{\rm eff} - 0.511$ MeV $> 5.0$ MeV, and a reconstructed position with $R_{\rm fit} < 550$ cm ($\rho < 0.77$).

For SNO Phase I to be able to make a measurement of the total flux of neutrinos via the NC reaction, it was critical that the number of background neutrons was small compared to those expected from solar neutrinos. The most dangerous source of such neutrons was those from the photodisintegration of deuterons by $\gamma$ rays, resulting from decays in the $^{238}$U and $^{232}$Th chains. The levels of U and Th were measured in two ways: *ex situ* assays of the heavy and light water [9, 10], and *in situ* measurements of $^{208}$Tl and $^{214}$Bi concentrations using the differences in the isotropy of their Cherenkov-light distributions. Both methods agreed well, and by combining them the levels of U and Th in the heavy water were found to be:

$$\begin{aligned} ^{232}\mathrm{Th} &: 1.61 \pm 0.58 \times 10^{-15} \text{g Th/g } D_2O \\ ^{238}\mathrm{U} &: 17.8^{+3.5}_{-4.3} \times 10^{-15} \text{ g U/g } D_2O. \end{aligned}$$

With these measurements, and those of radioactivity in the light water and acrylic vessel,

the total number of background neutrons from photodisintegration in the Phase-I data set was $38.2^{+9.4}_{-9.5}$ from the $^{232}$Th chain and $33.1^{+6.7}_{-7.1}$ from $^{238}$U chain. Neutrons from other sources, such as atmospheric neutrinos and $(\alpha, n)$ processes, were found to be just $7^{+3}_{-1}$ counts.

The PDFs shown in Fig. 3 were created via a calibrated and over-constrained Monte Carlo simulation. Events resulting from $^8$B neutrino interactions or sources of background were passed through a detector model that included the propagation of electrons, $\gamma$ rays, and neutrons through the heavy water, a detailed optical response of the detector media and PMTs, and data acquisition electronics. Parameters such as optical attenuation lengths, scattering, and overall PMT collection efficiency were measured by deploying a diffuse laser source [12] and a $^{16}$N source [6] of 6.1-MeV $\gamma$ rays throughout the detector volume. Residual differences between the model prediction for energy scale, energy resolution, vertex reconstruction bias and vertex resolution, were taken as systematic uncertainties on the model, and were within $\pm$ 1%. The overall neutron capture efficiency was measured using the deployment of a $^{252}$Cf source throughout the detector volume.

The fit to the data set using the PDFs of Fig. 3 was done via an extended log-likelihood of the form:

$$\log L = -\sum_i N_i + \sum_j n_j \ln\{\nu(T_{\mathrm{eff}j}, \rho_j, \cos\theta_{\odot j})\}, \tag{1}$$

where $N_i$ is the number of events of type $i$ (e.g. CC, ES, or NC), $j$ is a sum over all three-dimensional bins in the three signal extraction parameters $T_{\mathrm{eff}}$, $\rho$, and $\cos\theta_\odot$, and $n_j$ is the number of detected events in each bin. The numbers of CC, ES, and NC events were treated as free parameters in the fit. The likelihood function was maximized over the free parameters, and the best fit point yielded the number of CC, ES, and NC events along with a covariance matrix.

The Phase-I data set was fit under two different assumptions. The first was that the recoil electron spectra of the CC and ES events resulted from an undistorted $^8$B neutrino spectrum, thus testing the null hypothesis that solar neutrinos do not change flavor. The second fit had no such constraint, and could be done either by fitting events bin-by-bin in energy [13] or by using only $\rho$ and $\cos\theta_\odot$ [14].

In addition to fitting for the three signal rates (CC, ES, and NC), the SNO data also allowed a direct fit for the neutrino flavor content through a change of variables:

$$\phi_{\mathrm{CC}} = \phi(\nu_e) \tag{2}$$

$$\phi_{\mathrm{ES}} = \phi(\nu_e) + 0.1559\phi(\nu_{\mu\tau}) \tag{3}$$

$$\phi_{\mathrm{NC}} = \phi(\nu_e) + \phi(\nu_{\mu\tau}). \tag{4}$$

The factor of 0.1559 is the ratio of the ES cross sections for $\nu_{\mu\tau}$ and $\nu_e$ above $T_{\mathrm{eff}} = 5.0$ MeV. Making this change of variables and fitting directly for the flavor content, the null hypothesis test of no flavor change is reduced to a test of $\phi(\nu_{\mu\tau}) = 0$.

Conversion of event numbers from the fit into neutrino fluxes required corrections for cut acceptance, live time, measured neutron capture efficiency, subtraction of neutron backgrounds, and effects not included in the Monte Carlo simulation (such as the eccentricity of the Earth's orbit). With these corrections applied, and measurements of the systematic

uncertainties on both acceptances and detector response, the flux values for the constrained fit are (in units of $10^6$ cm$^{-2}$s$^{-1}$):

$$\phi_{\rm CC} = 1.76^{+0.06}_{-0.05}({\rm stat.})^{+0.09}_{-0.09}\ ({\rm syst.})$$
$$\phi_{\rm ES} = 2.39^{+0.24}_{-0.23}({\rm stat.})^{+0.12}_{-0.12}\ ({\rm syst.})$$
$$\phi_{\rm NC} = 5.09^{+0.44}_{-0.43}({\rm stat.})^{+0.46}_{-0.43}\ ({\rm syst.}).$$

The physical interpretation of the "flux" for each interaction type is that it is the equivalent flux of $^8$B $\nu_e$s produced from an undistorted energy spectrum that would yield the same number of events inside the signal region from that interaction as was seen in the data set.

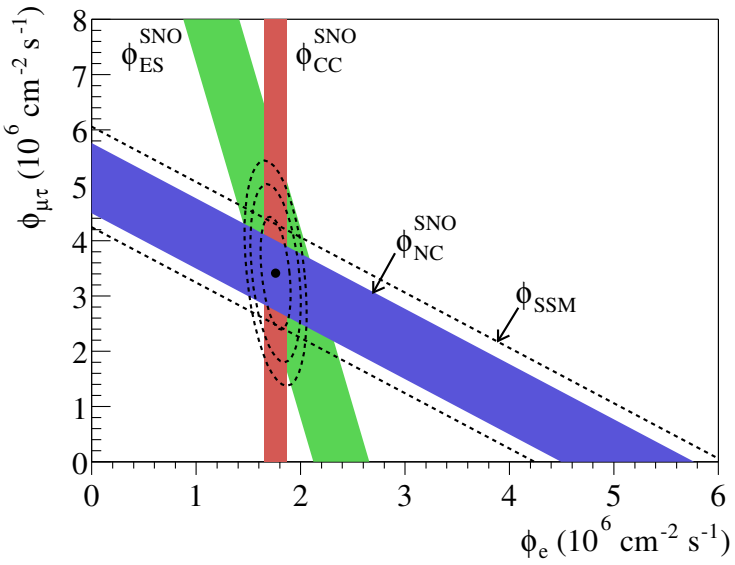


Figure 4: Flux of $^8$B solar neutrinos which are $\mu$ or $\tau$ flavor vs flux of electron neutrinos deduced from the three neutrino reactions in SNO. The diagonal bands show the total $^8$B flux as predicted by the BP2000 SSM [4] (dashed lines) and that measured with the NC reaction in SNO (solid band). The intercepts of these bands with the axes represent the $\pm1\sigma$ errors. The bands intersect at the fit values for $\phi_e$ and $\phi_{\mu\tau}$, indicating that the combined flux results are consistent with neutrino flavor transformation with no distortion in the $^8$B neutrino energy spectrum.

The inequality of the fluxes determined from the CC, ES, and NC reactions provided strong evidence for a non-$\nu_e$ component to the $^8$B solar neutrinos. Figure 4 shows the constraints on the flux of $\nu_e$ versus the combined $\nu_\mu$ and $\nu_\tau$ fluxes derived from the CC, ES, and NC rates. Together the three rates were inconsistent with the hypothesis that the $^8$B flux consists solely of $\nu_e$s, but are consistent with an admixture consisting of about 1/3 $\nu_e$ and 2/3 $\nu_\mu$ and/or $\nu_\tau$.

Changing variables to provide a direct measure of flavor content, the fluxes are (in units of $10^6$ cm$^{-2}$s$^{-1}$):

$$\phi(\nu_e) = 1.76^{+0.05}_{-0.05}({\rm stat.})^{+0.09}_{-0.09}\ ({\rm syst.})$$
$$\phi(\nu_{\mu\tau}) = 3.41^{+0.45}_{-0.45}({\rm stat.})^{+0.48}_{-0.45}\ ({\rm syst.}).$$

Adding the statistical and systematic errors in quadrature, $\phi(\nu_{\mu\tau})$ is $5.3\sigma$ away from its null hypothesis value of zero.

With the corrections applied and normalizing to the Monte Carlo event rates, the "NC flux" for the energy-unconstrained fit between $5 < T_{\rm eff} < 19.5$ MeV (using only $\rho$ and $\cos\theta_{\odot}$), was:

$$\phi_{\rm NC} = 6.42^{+1.57}_{-1.57}({\rm stat.})^{+0.55}_{-0.58}\ ({\rm syst.}) \times 10^6\ {\rm cm}^{-2}\ {\rm s}^{-1}.$$

Both measurements of the total active fluxes $\phi_{NC}$, as well as the sum of $\phi(\nu_e) + \phi(\nu_{\mu\tau})$, were in good agreement with Standard Solar Model predictions[4, 15]. Using the same data set, SNO did not observe any statistically significant day-night asymmetries of the CC, NC, and ES reaction rates [16].

These results for the full data set of Phase I were in good agreement with and more accurate than the results obtained [13] by comparison of the SNO CC data with ES data from Superkamiokande.

## 5. SNO Phase-II Physics Program

In Phase II, approximately 2000 kg of NaCl was dissolved in the 1000-tonne heavy-water neutrino target of SNO. The addition of salt enhanced the experiment's sensitivity to detect $^8$B solar neutrinos through the NC reaction in several ways. The thermal neutron capture cross section for $^{35}$Cl is nearly five orders of magnitude larger than that for the deuteron, resulting in a significant increase in the neutron capture efficiency in the detector. The $Q$-value for radiative neutron capture on $^{35}$Cl is 8.6 MeV, which is 2.3 MeV above that for capture on the deuteron. The increase in the released energy led to more observable NC events above the energy threshold ($T_{\rm eff} > 5.5$ MeV) in the measurement, but more importantly, the cascade of prompt $\gamma$ rays following neutron capture on $^{35}$Cl produced a Cherenkov-light hit pattern on the PMT array that was significantly different from that produced by a single relativistic electron from the CC or the ES reactions. Multiple $\gamma$ rays produced a more isotropic pattern of triggered PMTs on the PSUP. This difference in the observed event topology allowed the statistical separation between events from the NC and the CC reactions without making any assumption on the underlying neutrino energy spectrum.

The complete Phase-II data set consisted of $391.432 \pm 0.082$ live days of data recorded between July 26, 2001 and August 28, 2003. A blind analysis was performed on the initial 254.2-live-day data set in Ref. [17], followed by an analysis of the full data set in Ref. [18]. In the blind analysis, an unknown fraction of the data were excluded, and an unknown admixture of neutrons following cosmic muons events was added. An unknown scaling factor of the NC cross section was also applied to the simulation code. After fixing all analysis procedures and parameters, the blindness constraints were removed for a full analysis of the 254-live-day data set.

To exploit the difference in Cherenkov-light event topology for different types of signals, several variables were constructed. The variable that was eventually adopted, which could be

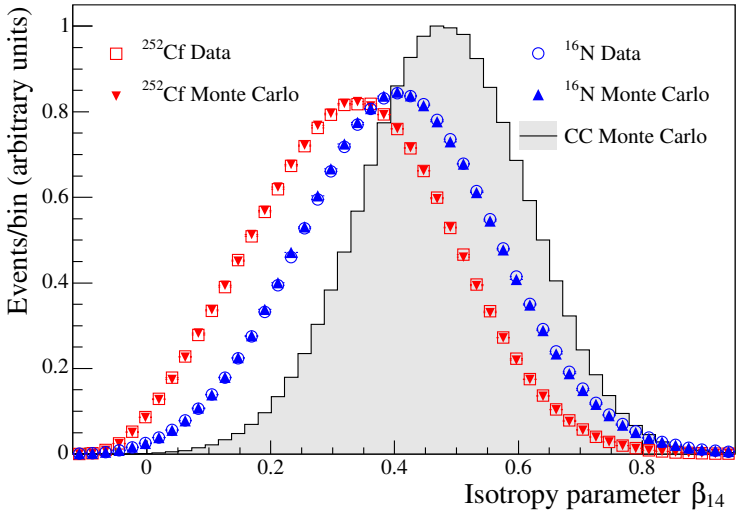


Figure 5: $\beta_{14}$ isotropy distributions for $^{252}$Cf data and MC, $^{16}$N data and simulations, and simulated CC events. Good agreement was found between simulated $\beta_{14}$ and $^{252}$Cf and $^{16}$N calibration data. Note that the distribution normalizations are arbitrary and chosen to allow the shape differences to be seen clearly.

simply parameterized and facilitated systematic uncertainty evaluations, was $\beta_{14} \equiv \beta_1 + 4\beta_4$ where

$$\beta_l = \frac{2}{N(N-1)} \sum_{i=1}^{N-1} \sum_{j=i+1}^{N} P_l(\cos\theta_{ij}). \tag{5}$$

In this expression $P_l$ is the Legendre polynomial of order $l$, $\theta_{ij}$ is the angle between triggered PMTs $i$ and $j$ relative to the reconstructed event vertex, and $N$ is the total number of triggered PMTs in the event. Figure 5 shows the difference in the $\beta_{14}$ distributions between neutron (NC) and electron (CC or ES) events.

The neutron response of the detector was calibrated primarily with neutrons produced by a $^{252}$Cf source with secondary checks made by analysis of neutrons generated by an Am-Be source and by Monte Carlo simulations. The volume-weighted detection efficiency for neutrons generated uniformly in the $D_2O$ for the analysis threshold of $T_{\rm eff} = 5.5$ MeV and a fiducial volume of 550 cm ($\rho < 0.77$) was found to be $0.407 \pm 0.005$ (stat.)$^{+0.009}_{-0.008}$ (syst.).

As in Phase I, a normalization for photon detection efficiency based on $^{16}$N [6] calibration data and Monte Carlo simulations was used to set the absolute energy scale. A $\sim$2% gain drift was observed in the $^{16}$N data taken throughout the running period; this drift was predicted by simulations based on temporal changes in the optical measurements. The overall energy-scale resolution uncertainty was found to be 1.15%.

Compared to Phase I, the addition of salt increased the sensitivity to neutron capture at large $\rho$, making it possible to detect background neutrons originating at or near the acrylic vessel and in the $H_2O$. In Phase I, the magnitude of these "external source" neutrons were estimated and fixed in the neutrino signal decomposition analysis. In Phase II, the amplitude of the $\rho$ PDF of the external source neutrons was allowed to vary in the maximum

likelihood fit.

In the determination of the electron-energy spectrum from CC and ES interactions and the total active solar neutrino flux, an extended maximum likelihood fit with four data variables ($T_{\rm eff}$, $\rho$, $\cos\theta_\odot$, and $\beta_{14}$) was performed. To obtain the electron energy spectra of CC and ES interactions, probability density functions (PDFs) were simulated for $T_{\rm eff}$ intervals, which spanned the range from 5.5 MeV to 13.5 MeV in 0.5 MeV steps. A single bin was used for $T_{\rm eff}$ values between 13.5 and 20 MeV. The $T_{\rm eff}$ PDFs for NC and external source neutrons were simply the detector's energy response to radiative neutron captures on $^{35}$Cl and $^{2}$H. Minor adjustments were applied to the PDFs to take into account signal loss due to instrumental cuts not modeled by the simulation. A four-dimensional PDF was implemented in the signal decomposition:

$$P(T_{\rm eff}, \beta_{14}, \rho, \cos\theta_\odot) = P(T_{\rm eff}, \beta_{14}, \rho) \times P(\cos\theta_\odot | T_{\rm eff}, \rho), \tag{6}$$

where the first factor is just the 3-dimensional PDF for the variables $T_{\rm eff}$, $\beta_{14}$, and $\rho$, while the second factor is the conditional PDF for $\cos\theta_\odot$, given $T_{\rm eff}$ and $\rho$. In the maximum likelihood fit the PDF normalizations for CC and ES components were allowed to vary separately in each $T_{\rm eff}$ bin to obtain their model-independent spectra. For the NC and external neutron components only their overall normalizations were allowed to vary. Figure 6 shows the extracted CC and ES electron energy spectra.

For this energy-unconstrained analysis, the integral neutrino flux were determined to be (in units of $10^6$ cm$^{-2}$s$^{-1}$):

$$\begin{aligned}
\phi_{\rm CC}^{\rm uncon} &= 1.68^{+0.06}_{-0.06}({\rm stat.})^{+0.08}_{-0.09}({\rm syst.}) \\
\phi_{\rm ES}^{\rm uncon} &= 2.35^{+0.22}_{-0.22}({\rm stat.})^{+0.15}_{-0.15}({\rm syst.}) \\
\phi_{\rm NC}^{\rm uncon} &= 4.94^{+0.21}_{-0.21}({\rm stat.})^{+0.38}_{-0.34}({\rm syst.}) \ ,
\end{aligned}$$

and the ratios of the CC flux to that of NC and ES are

$$\begin{aligned}
\frac{\phi_{\rm CC}^{\rm uncon}}{\phi_{\rm NC}^{\rm uncon}} &= 0.340 \pm 0.023 \ ({\rm stat.}) \ ^{+0.029}_{-0.031} \ ({\rm syst.}) \\
\frac{\phi_{\rm CC}^{\rm uncon}}{\phi_{\rm ES}^{\rm uncon}} &= 0.712 \pm 0.075 \ ({\rm stat.}) \ ^{+0.045}_{-0.044} \ ({\rm syst.}).
\end{aligned}$$

In a subsequent analysis of the combined Phase-I and Phase-II data sets [19], the energy threshold was lowered to $T_{\rm eff}$ >3.5 MeV (the lowest achieved with a water Cherenkov neutrino detector). Two different analysis methods, one based on binned histograms and another on kernel estimation, were developed in the joint analysis. With numerous improvements to background modeling, optical and energy response determination, and treatment of systematic uncertainties in the signal decomposition process, the uncertainty in the total active solar neutrino flux was reduced by more than a factor of two (in units of $10^6$ cm$^{-2}$s$^{-1}$):

$$\phi_{\rm NC}^{\rm uncon} = 5.140^{+0.160}_{-0.158}({\rm stat.})^{+0.132}_{-0.117}({\rm syst.}). \tag{7}$$

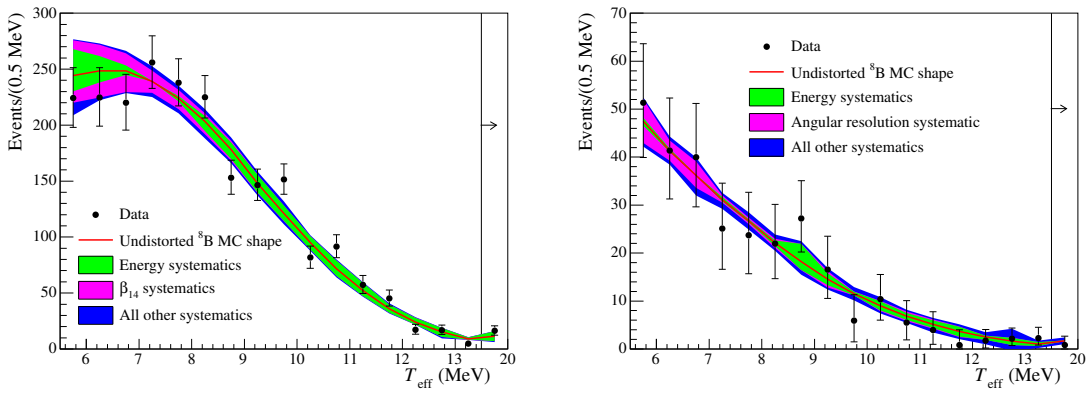


Figure 6: Left: Extracted CC $T_{\rm eff}$ spectrum with statistical error bars compared to predictions for an undistorted $^8$B shape with combined systematic uncertainties, including both shape and acceptance components. The highest-energy bin represents the average number of events per 0.5 MeV for the range of 13.5-20 MeV. Right: An analogous plot for the extracted ES $T_{\rm eff}$ spectrum.

If the unitarity condition is assumed (i.e. no transformation from active to sterile neutrinos), the CC, ES and NC rates are directly related to the total $^8$B solar neutrino flux. A signal decomposition fit was performed in this combined analysis in which the free parameters directly described the total $^8$B neutrino flux and the energy-dependent $\nu_e$ survival probability. In this scenario, the total $^8$B neutrino flux was found to be (in units of $10^6$ cm$^{-2}$s$^{-1}$):

$$\Phi_{^8\rm B} = 5.046^{+0.159}_{-0.152}(\text{stat.})^{+0.107}_{-0.123}(\text{syst.}). \tag{8}$$

Further details on this joint analysis and that for data from all three phases of the experiment can be found in Sec. 7.

## 6. SNO Phase-III Physics Program

In Phase III of the experiment, an array of $^3$He proportional counters [20] was deployed in the $D_2O$ volume. The neutron signal in the inclusive total active neutrino flux measurement was detected predominantly by this "Neutral-Current Detection" (NCD) array via

$$n + {}^3\text{He} \rightarrow p + t + 764 \text{ keV},$$

and was separate from the Cherenkov-light signals in the $\nu_e$ flux measurement. The separation resulted in reduced correlations between the total active neutrino flux and $\nu_e$ flux measurements, and therefore the measurement of the total active $^8$B solar neutrino flux was largely independent of the methods of previous phases.

The NCD array consisted of 36 strings of $^3$He and 4 strings of $^4$He proportional counters, which were deployed on a square grid with 1-m spacing [20]. The $^4$He strings were not sensitive to neutrons and were used for characterizing non-neutron backgrounds. Each detector string was made up of three or four individual 5-cm-diameter counters that were

laser-welded together. The counters were constructed from ultra-pure nickel produced by a chemical deposition process to minimize internal radioactivity. Figure 7 shows a side view of the SNO detector with the NCD array in place.

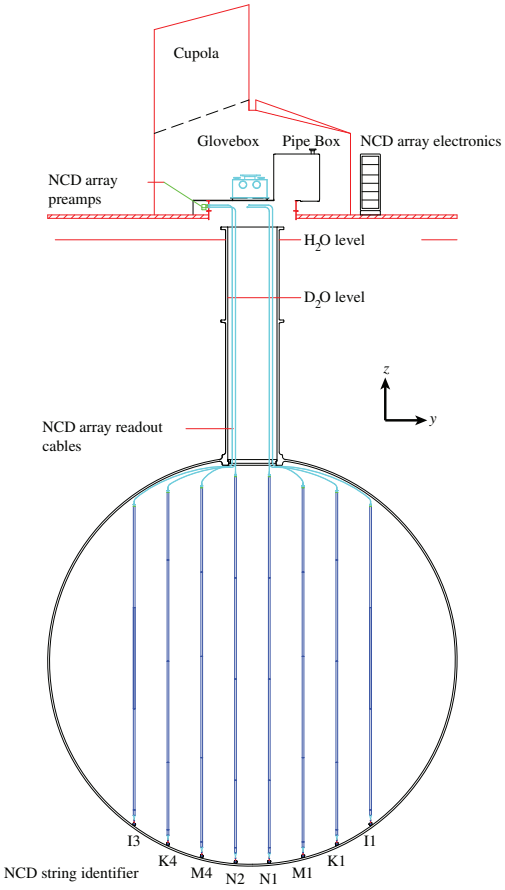


Figure 7: Side view of the SNO detector in Phase III. Only the first row of NCD strings from the $y-z$ plane are displayed in this figure.

The Phase-III data set represented $385.17 \pm 0.14$ live days of data recorded between November 27, 2004 and November 28, 2006. During this period, the SNO detector was live nearly 90% of the time, with approximately 30% of the live time spent on detector calibration. Six $^3$He strings were defective and their data were excluded in the measurement.

In Phase III, optical and energy calibration procedures, as well as Cherenkov-event reconstruction, were modified from those in previous phases to account for the optical complexity introduced by the NCD array. Similar to previous phases, the primary source for energy scale and resolution calibration of the PMT array was the $^{16}$N source [6]. In Phase III, the energy scale uncertainty was found to be 1.04%.

The NCD array had two independently triggered readout systems, a fast shaper system that recorded signal peak heights and could operate at high rates in the event of a galactic supernova, and a slower, full waveform digitization system that had a 15-$\mu$s window around

the signal. The detector signal response to neutrons was calibrated using Am-Be neutron source data.

The principal method for determining the neutron detection efficiency of the PMT and NCD arrays was to deploy an evenly distributed $^{24}$Na source in the $D_2O$ [21]. The source was deployed by injecting a neutron-activated brine throughout the volume. The $\gamma$s created by the $^{24}$Na then created free neutrons through photodisintegration of deuterons in the heavy water. Thus neutron capture efficiency determined this way was found to be $\epsilon = 0.211 \pm 0.005$. Additional corrections for threshold and other effects reduced the overall detection efficiency to 86.2% of this value.

A small fraction of NC neutrons was captured by the deuterons in the target, resulting in the emission of a 6.25-MeV $\gamma$ ray that could be detected by the PMT array. The efficiency for the detection of these events was $0.0502 \pm 0.0014$.

The evaluation of the intrinsic radioactive backgrounds in the detector construction materials and in the $D_2O$ and $H_2O$ volumes followed analogous procedures in previous phases, with adjustments for the added optical complexity of the detector, and with new analyses developed to measure backgrounds on the NCDs themselves. These analyses used both information from Cherenkov light and signals from the NCD counters, and the two techniques were in good agreement. Two radioactive "hot spots" were identified on two separate NCD strings from the Cherenkov-light signals. An extensive experimental program was developed to measure the radioactive content of these hot spots. More details can be obtained from Ref. [22].

Like Phases I and II, extraction of the neutrino signals for Phase III used an extended maximum likelihood fit to data, which for this phase included both PMT (Cherenkov) signals and the summed energy spectrum from the NCD shaper data ("shaper energy", $E_{\rm NCD}$). The fit to the shaper energy included an alpha background distribution [23] from simulation, a neutron spectrum determined from $^{24}$Na calibration source data, expected neutron backgrounds, and instrumental background event distributions. The same blindness approach was used here as in Phase II.

The negative log-likelihood (NLL) function to be minimized was the sum of a NLL for the PMT array data ($-\log L_{\rm PMT}$) and for the NCD array data ($-\log L_{\rm NCD}$). The spectral distributions of the ES and CC events were not constrained to the $^8$B shape in the fit, but were extracted from the data. It should be noted that the $^8$B spectral shape used here [24] differed from that used in previous phases [25]. Figure 8 shows the one-dimensional projection of the NCD array data overlaid with the best-fit results to signals. The energy-unconstrained NC flux results from Phase III are in good agreement which those in previous phases, as shown in Fig. 9. It should be emphasized that the energy-unconstrained solar neutrino flux measurements are independent of solar model inputs.

A detailed description of SNO's Phase-III solar-neutrino measurements can be found in Refs. [27, 28].

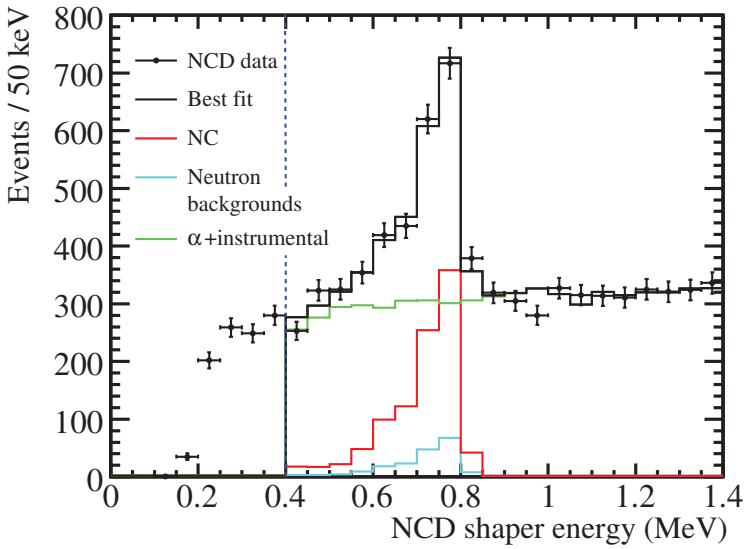


Figure 8: One-dimensional projection of NCD-array shaper-energy data overlaid with best-fit results for the NC signal as well as for the neutron, alpha and instrumental backgrounds.

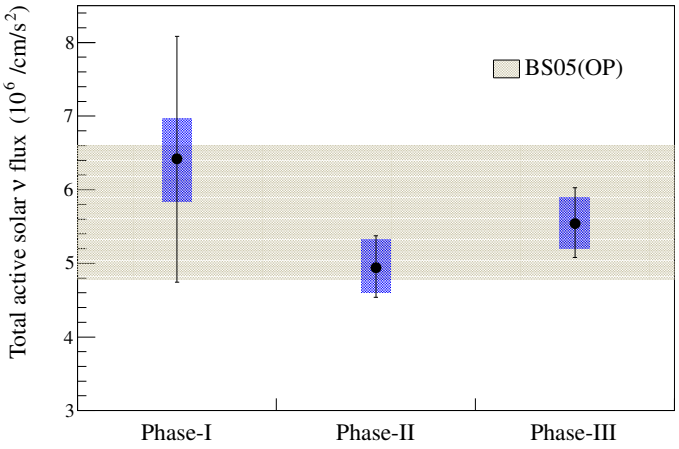


Figure 9: A comparison of the measured energy-unconstrained NC flux results in SNO's three phases. The error bars represent the total $\pm 1\sigma$ uncertainty for the measurements, while the height of the shaded boxes represents that for the systematic uncertainties. The horizontal band is the $1\sigma$ region of the expected total $^8$B solar neutrino flux in the BS05(OP) model [26].

## 7. Combined Analysis of all Three Phases

The most precise values for the solar neutrino mixing parameters and the total flux of $^8$B neutrinos from the Sun resulted from a joint analysis of data from all three phases of the SNO experiment [29]. The joint analysis accounted for correlations in systematic uncertainties between phases, and was based on two distinct strategies. The first was to push toward the lowest energy threshold possible as it was done in the low-energy threshold analysis [19] described at the end of Sec. 5, while the second was to strongly leverage the two independent detection techniques afforded by the combination of Cherenkov-light data from all three phases and NCD counter data from Phase III. The combination of all phases therefore provided a statistically powerful separation of CC, ES and NC events, and two independent ways to measure the total flux of active-flavor neutrinos from $^8$B decay in the Sun.

The data were split into day and night sets in order to search for matter effects as the neutrinos propagated through the Earth. The results of the analysis were presented in the same form as the low-energy threshold analysis [19], providing the total $^8$B neutrino flux, $\Phi_{\rm B}$, independently of any specific active neutrino flavor oscillation hypothesis; and the energy-dependent $\nu_e$ survival probability describing the probability that an electron neutrino remains an electron neutrino in its journey between the Sun and the SNO detector. The parameterization of the $^8$B neutrino signal was based on an average $\Phi_{\rm B}$ for day and night, a $\nu_e$ survival probability as a function of neutrino energy, $E_\nu$, during the day, $P^{\rm d}_{ee}(E_\nu)$, and an asymmetry between the day and night survival probabilities, $A_{ee}(E_\nu)$. It was defined as

$$\begin{aligned} P^{\rm d}_{ee}(E_\nu) &= c_0 + c_1(E_\nu[\mathrm{MeV}] - 10) \\ &\quad + c_2(E_\nu[\mathrm{MeV}] - 10)^2 \end{aligned} \tag{9}$$

and

$$A_{ee}(E_\nu) = 2\frac{P^{\rm n}_{ee}(E_\nu) - P^{\rm d}_{ee}(E_\nu)}{P^{\rm n}_{ee}(E_\nu) + P^{\rm d}_{ee}(E_\nu)}, \tag{10}$$

where $P^{\rm n}_{ee}(E_\nu)$ is the $\nu_e$ survival probability during the night and with

$$A_{ee}(E_\nu) = a_0 + a_1(E_\nu[\mathrm{MeV}] - 10). \tag{11}$$

The parameters $a_0$, and $a_1$ define the relative difference between the night and day $\nu_e$ survival probability; while $c_0$, $c_1$, and $c_2$ define the $\nu_e$ survival probability during the day. In this parametrization the $\nu_e$ survival probability during the night is given by

$$P^{\rm n}_{ee}(E_\nu) = P^{\rm d}_{ee}(E_\nu) \times \frac{1 + A_{ee}(E_\nu)/2}{1 - A_{ee}(E_\nu)/2}. \tag{12}$$

As with solar neutrino analyses described in previous sections, a maximum likelihood fit was performed to the Cherenkov events $T_{\rm eff}$, $\rho = (R/R_{AV})^3$, $\beta_{14}$, and $\cos\theta_\odot$. The "shaper energy", $E_{\rm NCD}$, was calculated for each event recorded with the NCD array. Monte Carlo

simulations assuming the Standard Solar Model and no neutrino oscillations were used to determine the event variables for $^8$B neutrino interactions in the detector.

In the final fit, the events observed in the PMT and NCD arrays were treated as being uncorrelated, therefore the negative log-likelihood (NLL) function for all data were given by

$$-\log L_{\rm data} = -\log L_{\rm PMT} - \log L_{\rm NCD}, \tag{13}$$

where $L_{\rm PMT}$ and $L_{\rm NCD}$, respectively, were the likelihood functions for the events observed in the PMT and NCD arrays. The NLL function in the PMT array was given by

$$-\log L_{\rm PMT} = \sum_{j=1}^{N} \lambda_j(\vec{\eta}) - \sum_{i=1}^{n_{\rm PMT}} \log \left[ \sum_{j=1}^{N} \lambda_j(\vec{\eta}) f(\vec{x}_i|j,\vec{\eta}) \right], \tag{14}$$

where $N$ was the number of different event classes, $\vec{\eta}$ was a vector of "nuisance" parameters associated with the systematic uncertainties, $\lambda_j(\vec{\eta})$ was the mean of a Poisson distribution for the $j^{\rm th}$ class, $\vec{x}_i$ was the vector of event variables for event $i$, $n_{\rm PMT}$ was the total number of events in the PMT array during the three phases, and $f(\vec{x}_i|j,\vec{\eta})$ was the PDF for events of type $j$. The PDFs for the signal events were re-weighted based on Eqns. 9 and 11. The NLL function in the NCD array was given by

$$-\log L_{\rm NCD} \;=\; \frac{1}{2}\left( \frac{\sum_{j=1}^{N} \nu_j(\vec{\eta}) - n_{\rm NCD}}{\sigma_{\rm NCD}} \right)^2, \tag{15}$$

where $\nu_j(\vec{\eta})$ was the mean of a Poisson distribution for the $j^{\rm th}$ class, $n_{\rm NCD}$ was the total number of neutrons observed in the NCD array based on the likelihood fit to a histogram of $E_{\rm NCD}$, and $\sigma_{\rm NCD}$ was the associated uncertainty.

Table 1: Results from the maximum likelihood fit. Note that $\Phi_{\rm B}$ is in units of $\times 10^6\,{\rm cm}^{-2}{\rm s}^{-1}$. The D/N systematic uncertainties include the effect of all nuisance parameters that were applied differently between day and night. The MC systematic uncertainties include the effect of varying the number of events in the Monte Carlo based on Poisson statistics. The basic systematic uncertainties include the effects of all other nuisance parameters.

| | Best fit | Stat. | Systematic uncertainty | | | |
|---|---|---|---|---|---|---|
| | | | Basic | D/N | MC | Total |
| $\Phi_{\rm B}$ | 5.25 | $\pm$0.16 | $^{+0.11}_{-0.12}$ | $\pm$0.01 | $^{+0.01}_{-0.03}$ | $^{+0.11}_{-0.13}$ |
| $c_0$ | 0.317 | $\pm$0.016 | $^{+0.008}_{-0.010}$ | $\pm$0.002 | $^{+0.002}_{-0.001}$ | $\pm$0.009 |
| $c_1$ | 0.0039 | $^{+0.0065}_{-0.0067}$ | $^{+0.0047}_{-0.0038}$ | $^{+0.0012}_{-0.0018}$ | $^{+0.0004}_{-0.0008}$ | $\pm$0.0045 |
| $c_2$ | -0.0010 | $\pm$0.0029 | $^{+0.0013}_{-0.0016}$ | $^{+0.0002}_{-0.0003}$ | $^{+0.0004}_{-0.0002}$ | $^{+0.0014}_{-0.0016}$ |
| $a_0$ | 0.046 | $\pm$0.031 | $^{+0.007}_{-0.005}$ | $\pm$0.012 | $^{+0.002}_{-0.003}$ | $^{+0.014}_{-0.013}$ |
| $a_1$ | -0.016 | $\pm$0.025 | $^{+0.003}_{-0.006}$ | $\pm$0.009 | $\pm$0.002 | $^{+0.010}_{-0.011}$ |

The final joint fit to all data yielded a total flux of active neutrino flavors from $^8$B decays in the Sun of $\Phi_{\rm B}$=$(5.25 \pm 0.16({\rm stat.})^{+0.11}_{-0.13}({\rm syst.})) \times 10^6\,{\rm cm}^{-2}{\rm s}^{-1}$. During the day the

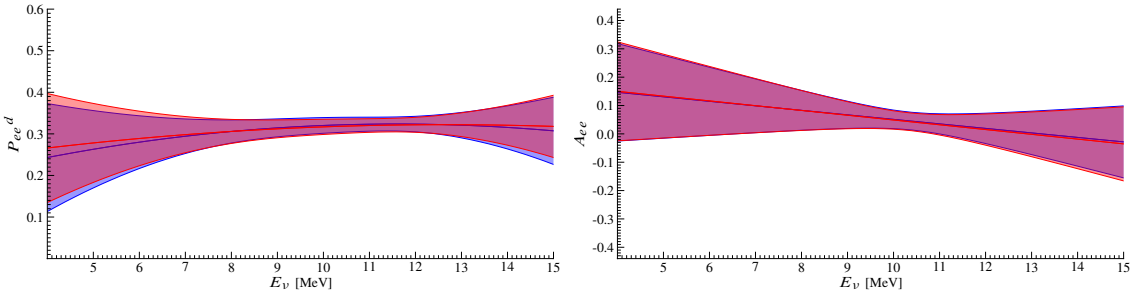


Figure 10: Root-mean-square spread in $P_{ee}^{\rm d}(E_\nu)$ (left) and $A_{ee}(E_\nu)$ (right), taking into account the parameter uncertainties and correlations. The red band represents the results from the maximum likelihood fit, and the blue band represents the results from the Bayesian fit. The red and blue solid lines, respectively, are the best fits from the maximum likelihood and Bayesian fits.

$\nu_e$ survival probability at 10 MeV was given by $c_0 = 0.317 \pm 0.016(\text{stat.}) \pm 0.009(\text{syst.})$, which was inconsistent with the null hypothesis that there were no neutrino oscillations at very high significance. The results of the combined fit for $\Phi_{\rm B}$ and the $\nu_e$ survival probability parameters are summarized in Table 1. The null hypothesis that there were no spectral distortions of the $\nu_e$ survival probability (i.e. $c_1 = 0$, $c_2 = 0$, $a_0 = 0$, $a_1 = 0$), yielded $\Delta\chi^2 = 1.97$ (26% C.L) compared to the best fit. The null hypothesis that there were no day/night distortions of the $\nu_e$ survival probability (i.e. $a_0 = 0$, $a_1 = 0$), yielded $\Delta\chi^2 = 1.87$ (61% C.L.) compared to the best fit.

Figure 10 shows the root-mean-square spread in $P_{ee}^{\rm d}(E_\nu)$ and $A_{ee}(E_\nu)$, taking into account the parameter uncertainties and correlations. A Bayesian approach was used as validation analysis and details of this combined analysis are described in Ref. [29].

## 8. Neutrino Oscillations

The mass differences $\Delta m^2_{ij}$ and the mixing angles $\theta_{ij}$, obtained from neutrino experiments of different source-detector baselines, are used to parametrize the neutrino survival probabilities. Predicting the flux and energy spectrum ($E_\nu$) for all neutrino flavors requires a model of the neutrino production rates as a function of location within the Sun, and a model of the survival probabilities as the neutrinos propagate through the Sun, travel to the Earth, and then propagate through the Earth. When neutrinos travel through matter, the survival probabilities are modified due to the Mikheyev-Smirnov-Wolfenstein (MSW) effect [30, 31]. For consistency with previous calculations, the BS05(OP) model [26] was used for the solar neutrino production rate within the Sun, rather than the more recent BPS09(GS) or BPS09(AGSS09) models [32]. The $E_\nu$ spectrum for $^8$B neutrinos was obtained from Ref. [24], while all other neutrino energy spectra were acquired from Ref. [33]. The electron density as a function of Earth radius was taken from PREM [34] and PEM-C [35].

Two different neutrino oscillation hypotheses were considered: 1) the historical two-flavor neutrino oscillations, which assumed $\theta_{13} = 0$ and had two free neutrino oscillation parameters, $\theta_{12}$ and $\Delta m^2_{21}$; and 2) the three-flavor neutrino oscillations, which fully integrated three

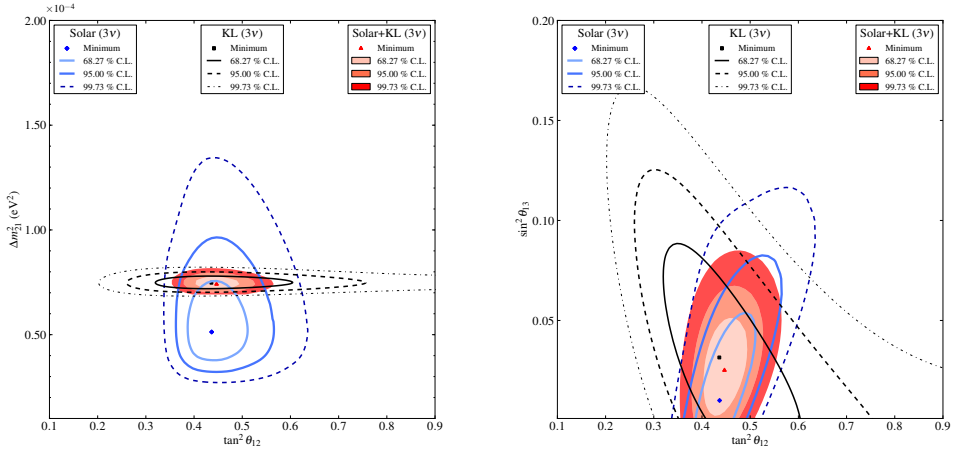


Figure 11: Three-flavor neutrino oscillation analysis contour using both solar neutrino and KamLAND (KL) results.

free neutrino oscillation parameters, $\theta_{12}$, $\theta_{13}$, and $\Delta m^2_{21}$. The mixing angle, $\theta_{23}$, and the CP-violating phase, $\delta$, are irrelevant for the neutrino oscillation analysis of solar neutrino data. The solar neutrino data considered here was insensitive to the exact value $\Delta m^2_{31}$, so we used a fixed value of $\pm 2.45 \times 10^{-3}\,\mathrm{eV}^2$ obtained from long-baseline accelerator experiments and atmospheric neutrino experiments [36]. The details of the oscillation analysis presented here is described in Ref. [29].

For the two-flavor analysis, Table 2 shows the allowed ranges of the $(\tan^2\theta_{12}, \Delta m^2_{21})$ parameters obtained with the SNO results. SNO data alone could not distinguish between the LMA region and the LOW region, although the former was slightly favored. The combination of the SNO results with the other solar neutrino experimental results eliminated the LOW region and the higher values of $\Delta m^2_{21}$ in the LMA region. Table 2 summarizes the results from these two-flavor neutrino analyses when the solar neutrino results were combined with those from the KamLAND (KL) reactor neutrino experiment [37].

Figure 11 shows the allowed regions in the $(\tan^2\theta_{12}, \Delta m^2_{21})$ and $(\tan^2\theta_{12}, \sin^2\theta_{13})$ parameter spaces obtained from the results of all solar neutrino experiments, as well as those including the results of the KamLAND experiment, in the three-flavor analysis. A non-zero $\theta_{13}$ has brought the solar neutrino results into better agreement with the results from the KamLAND experiment. Table 3 summarizes the results from these three-flavor neutrino oscillation analyses. Overall, the observation by SNO that the average solar $\nu_e$ survival probability at high energy is about 0.32 and $\theta_{12} \approx 33.5^\circ$ corroborate the matter-induced oscillation scenario of LMA via adiabatic conversion of electron neutrinos in the core of the Sun.

Table 2: Best-fit neutrino oscillation parameters from a two-flavor neutrino oscillation analysis. Uncertainties listed are $\pm 1\sigma$ after the $\chi^2$ was minimized with respect to all other parameters.

| Oscillation analysis | $\tan^2\theta_{12}$ | $\Delta m^2_{21}[\mathrm{eV}^2]$ | $\chi^2/\mathrm{NDF}$ |
|---|---|---|---|
| SNO only (LMA) | $0.427^{+0.033}_{-0.029}$ | $5.62^{+1.92}_{-1.36}\times 10^{-5}$ | $1.39/3$ |
| Solar | $0.427^{+0.028}_{-0.028}$ | $5.13^{+1.29}_{-0.96}\times 10^{-5}$ | $108.07/129$ |
| Solar+KamLAND | $0.427^{+0.027}_{-0.024}$ | $7.46^{+0.20}_{-0.19}\times 10^{-5}$ | |

Table 3: Best-fit neutrino oscillation parameters from the three-flavor neutrino oscillation analysis in Ref. [29]. Uncertainties listed are $\pm 1\sigma$ after the $\chi^2$ was minimized with respect to all other parameters. The global analysis includes solar neutrino experiments, KamLAND (KL) [38], and short baseline (SBL) experiments (Daya Bay [39], RENO [40], and Double Chooz [41]).

| Analysis | $\tan^2\theta_{12}$ | $\Delta m^2_{21}[\mathrm{eV}^2]$ | $\sin^2\theta_{13}(\times 10^{-2})$ |
|---|---|---|---|
| Solar | $0.436^{+0.048}_{-0.036}$ | $5.13^{+1.49}_{-0.98}\times 10^{-5}$ | $< 5.8$ (95% C.L.) |
| Solar+KL | $0.443^{+0.033}_{-0.026}$ | $7.46^{+0.20}_{-0.19}\times 10^{-5}$ | $2.5^{+1.8}_{-1.4}$ |
| | | | $< 5.3$ (95% C.L.) |
| Global (Solar+KL+SBL) | $0.443^{+0.030}_{-0.025}$ | $7.46^{+0.20}_{-0.19}\times 10^{-5}$ | $2.49^{+0.20}_{-0.32}$ |

## 9. Other Physics Studies

In addition to the solar neutrino measurements that led to the discovery of neutrino flavor transformation, the SNO data were also used to test various aspects of solar models and neutrino properties, and to search for neutrinos from astrophysical sources. Neutrinos from the *hep* reaction $^3\mathrm{H}+p \rightarrow {}^4\mathrm{He}+e^+ +\nu_e$ has an endpoint energy of 18.77 MeV, but its flux is predicted to be about three orders of magnitude lower than that of $^8$B neutrinos. Using the Phase-I data set (0.65 ktons yr exposure), an upper limit of $2.3\times 10^4$ cm$^{-2}$s$^{-1}$ (90% CL) was inferred on the integral total flux of *hep* neutrinos after neutrino oscillations had been taken into account [42]. In the same study, a search for the diffuse supernova neutrino background (DSNB), which consists of neutrinos from all extragalactic supernovae since the formation of stars in the Universe, was performed. An upper limit of 70 cm$^{-2}$ s$^{-1}$(90% CL) was found for the $\nu_e$ component of the DSNB flux in the neutrino energy range of 22.9 MeV$< E_\nu <$36.9 MeV. Although this is the most stringent limit on $\nu_e$ flux for direct measurements, the Super-Kamiokande experiment has reached an upper limit of 2.9 cm$^{-2}$ s$^{-1}$ for the $\bar{\nu}_e$ component [43]. An analysis to extend these analyses for the total three-phase data set is in progress.

The nuclear fusion rate in the solar core should not be affected by solar rotation or oscillations. To test this hypothesis, searches on the periodic variations in $^8$B solar neutrino flux were performed using Phase-I and Phase-II data sets. The analysis demonstrated that the fluctuation of $^8$B neutrino flux was consistent with modulation by the Earth's orbital eccentricity, and there were no significant sinusoidal periodicities found with periods between 1 d and 10 years [44]. Searches for high-frequency signals or extra power in the frequency range of 1 to 144 d$^{-1}$ did not detect any significant signal [45]. Additionally a search in the restricted frequency range of 18.5 to 19.5 d$^{-1}$, in which "gravitational-mode" ($g$-mode)

signals had been claimed in other experiments, did not show any signal.

Although the SNO detector did not observe any large burst of neutrino events that would be indicative of a galactic supernova explosion, a thorough study to search for low-multiplicity bursts, defined as bursts of two or more events that triggered the SNO detector in quick succession, was performed to look for evidence of distant supernovae or non-standard supernovae with relatively low neutrino emission [46]. The search had a greater than 50% detection probability for standard supernovae occurring at a distance of up to 60 kpc for Phase I and up to 70 kpc for Phase II. No low-multiplicity bursts were observed. The correlations of low-energy signals in the SNO detector and other astrophysical events, such as gamma-ray bursts and solar flares, were also studied [47]. No such correlations were found.

The great depth at which the SNO detector was located provided a unique opportunity to study cosmic-ray and neutrino-induced through-going muons. SNO measured the through-going muon flux as a function of the zenith angles ($\cos\theta_{\rm zenith}$), and was sensitive to neutrino-induced through-going muons in $-1 \leq \cos\theta_{\rm zenith} \leq 0.4$, i.e. including angles above the horizon [48]. Total cosmic-ray muon flux at SNO with $\cos\theta_{\rm zenith} > 0.4$ was found to be (3.31$\pm$0.01 (stat.)$\pm$0.09 (syst.))$\times 10^{-10} \mu$/s/cm$^2$. The zenith angle distribution of events ruled out the case of no neutrino oscillations at the $3\sigma$ level. This was the first measurement of the neutrino-induced flux above the horizon in the angular regime where neutrino oscillations were not an important effect.

The SNO data were also used to hunt for other new physics. Using the data from Phases I and II, SNO was able to constrain the lifetime for nucleon decay to "invisible" modes (such as $n \to 3\nu$) to $> 2 \times 10^{29}$ y [49] . This was accomplished by looking for $\gamma$ rays from the de-excitation of the residual nucleus that would result from the disappearance of either a proton or neutron from $^{16}$O. Non-standard-model physics, such as spin flavor precession mechanism or neutrino decays, could potentially convert a small fraction of solar $\nu_e$ to $\bar{\nu}_e$. The results from a search for $\bar{\nu}_e$ in Phase I [50] confirmed previous results from similar searches in the Super-Kamiokande [51] and KamLAND experiments [52]. An analysis of $\bar{\nu}_e$ with the full data set is in progress.

## 10. Summary

The principal results from SNO for solar neutrinos show clearly that electron neutrinos from $^8$B decay in the solar core change their flavor in transit to Earth. They also provide a measure of the total flux of $^8$B neutrinos with an accuracy that is better than the uncertainties in solar models and hopefully will provide guidance in our detailed understanding of the Sun. The SNO measurements of the flavor content of $^8$B solar neutrinos, along with measurements of different energy thresholds in other solar neutrino experiment, have provided much constraints on $\theta_{12}$, which is unlikely to improve further until a dedicated medium-baseline reactor neutrino experiment is online.

## 11. Acknowledgements

This research was supported by: Canada: Natural Sciences and Engineering Research Council, Industry Canada, National Research Council, Northern Ontario Heritage Fund, Atomic Energy of Canada, Ltd., Ontario Power Generation, High Performance Computing Virtual Laboratory, Canada Foundation for Innovation, Canada Research Chairs; US: Department of Energy, National Energy Research Scientific Computing Center, Alfred P. Sloan Foundation; UK: Science and Technology Facilities Council; Portugal: Fundação para a Ciência e a Tecnologia. We thank the SNO technical staff for their strong contributions. We thank Vale (formerly Inco, Ltd.) for hosting this project.

## References

[1] J.N. Bahcall, Neutrino Astrophysics, Cambridge University Press (1989).
[2] H. H. Chen, Phys. Rev. Lett. **55**, 1534 (1985).
[3] D. Sinclair, A.L. Carter, D. Kessler, E.D. Earle, P. Jagam, J.J. Simpson, R.C. Allen, H.H. Chen, P.J. Doe, E.D. Hallman, W.F. Davidson, A.B. McDonald, R.S. Storey, G.T. Ewan, H.B. Mak, B.C. Robertson, Il Nuovo Cimento C **9**, 308 (1986).
[4] J.N. Bahcall, M.H. Pinsonneault, and S. Basu, Astrophys. J. **555**, 990(2001).
[5] J. Boger *et al.* (SNO Collaboration), Nucl. Instr. and Meth. A **449**, 172(2000).
[6] M.R. Dragowsky *et al.*, Nucl. Inst. Meth. A **481**, 284 (2002).
[7] N.J. Tagg *et al.*, Nucl. Instr. and Meth. A **489**, 178(2002).
[8] A.W.P. Poon *et al.*, Nucl. Instr. and Meth. A **452**, 115(2000).
[9] T. C. Andersen *et al.*, Nucl. Instr. and Meth. A **501**, 399 (2003).
[10] T. C. Andersen *et al.*, Nucl. Instr. and Meth. A **501**, 386 (2003).
[11] B. Aharmim *et al.* (SNO Collaboration), Phys. Rev. C **75**, 045502 (2007).
[12] B. A. Moffat *et al.*, Nucl. Inst. Meth. A **554**, 255 (2005).
[13] Q. R. Ahmad *et al.* (SNO Collaboration), Phys. Rev. Lett. **87**, 071301 (2001).
[14] Q. R. Ahmad *et al.* (SNO Collaboration), Phys. Rev. Lett. **89**, 011301 (2002).
[15] A.S. Brun, S. Turck-Chièze, and J.P. Zahn, Astrophys. J. **525**, 1032(2001).
[16] Q.R. Ahmad *et al.* (SNO Collaboration), Phys. Rev. Lett. **89**, 011302 (2002).
[17] S.N. Ahmed *et al.* (SNO Collaboration), Phys. Rev. Lett. **92**, 181301 (2004).
[18] B. Aharmim *et al.* (SNO Collaboration), Phys. Rev. C **72**, 055502 (2005).
[19] B. Aharmim *et al.* (SNO Collaboration), Phys. Rev. C **81**, 055504 (2010).
[20] J. Amsbaugh *et al.*, Nucl. Inst. Meth. A **579**, 1054 (2007).
[21] K. Boudjemline *et al.*, Nucl. Instr. Meth. A **620**, 171 (2010).
[22] H. M. O'Keeffe *et al.*, Nucl. Inst. Meth. A **659**, 182 (2011).
[23] B. Beltran *et al.*, New J. Phys. **13**, 073006 (2011).
[24] W.T. Winter *et al.*, Phys. Rev. C **73**, 025503 (2006).
[25] C.E. Ortiz *et al.*, Phys. Rev. Lett. **85**, 2909 (2000).
[26] J. N. Bahcall, A. M. Serenelli, and S. Basu, Astrophys. J. **621**, L85 (2005).
[27] B. Aharmim *et al.* (SNO Collaboration), Phys. Rev. Lett. **101**, 111301 (2008).
[28] B. Aharmim *et al.* (SNO Collaboration), Phys. Rev. C **87**, 015502 (2013).
[29] B. Aharmim *et al.* (SNO Collaboration), Phys. Rev. C **88**, 025501 (2013).
[30] S. P. Mikheyev and A. Y. Smirnov, Nuovo Cim. C **9**, 17 (1986).
[31] L. Wolfenstein, Phys. Rev. D **17**, 2369 (1978).
[32] A. M. Serenelli, S. Basu, J. W. Ferguson, and M. Asplund, Astrophys. J. Lett. **705**, L123 (2009).
[33] `http://www.sns.ias.edu/$\sim$jnb/SNdata/sndata.html`
[34] A. M. Dziewonski and D. L. Anderson, Phys. Earth Planet. In. **25**, 297 (1981).
[35] A. M. Dziewonski, A. L. Hales, and E. R. Lapwood, Phys. Earth Planet. In. **10**, 12 (1975).

[36] T. Schwetz, M. Tórtola, and J. W. F. Valle, New J. Phys. **13**, 063004 (2011)
[37] S. Abe *et al.* (KamLAND Collaboration), Phys. Rev. C **84**, 035804 (2011).
[38] A. Gando *et al.* (KamLAND Collaboration) Phys. Rev. D **83**, 052002 (2011).
[39] F.P. An *et al.* (Daya Bay Collaboration), Chinese Physics C **37**, 011001 (2013).
[40] J.K. Ahn *et al.* (RENO Collaboration), Phys. Rev. Lett. **108**, 191802 (2012).
[41] Y. Abe *et al.* (Double Chooz Collaboration), Phys. Rev. Lett. **108**, 131801 (2013).
[42] B. Aharmim *et al.* (SNO Collaboration), Astrophys. J. **653**, 1545 (2006).
[43] K. Bays *et al.* (Super-Kamiokande Collaboration), Phys. Rev. D **85**, 052007 (2012).
[44] B. Aharmim *et al.* (SNO Collaboration), Phys. Rev. D **72**, 052010 (2005).
[45] B. Aharmim *et al.* (SNO Collaboration), Astrophys. J. **710**, 540 (2010).
[46] B. Aharmim *et al.* (SNO Collaboration), Astrophys. J. **728**, 83 (2011).
[47] B. Aharmim *et al.* (SNO Collaboration), Astropart. Phys. **55**, 1 (2014).
[48] B. Aharmim *et al.* (SNO Collaboration), Phys. Rev. D **80**, 012001 (2009).
[49] S.N. Ahmed *et al.* (SNO Collaboration), Phys. Rev. Lett. **92**, 102004 (2004).
[50] B. Aharmim *et al.* (SNO Collaboration), Phys. Rev. D **70**, 093014 (2004).
[51] Y. Gando *et al.* (Super-Kamiokande Collaboration), Phys. Rev. Lett. **90**, 171302 (2003).
[52] K. Eguchi *et al.* (KamLAND Collaboration), Phys. Rev. Lett. **92**, 071301 (2004).